

# Are observed H I filaments turbulent fraud or density structures?

## Velocity caustics, facts and fakes

P. M. W. Kalberla<sup>1</sup> and U. Haud<sup>2</sup>

<sup>1</sup> Argelander-Institut für Astronomie, Auf dem Hügel 71, 53121 Bonn, Germany  
 e-mail: pkalberla@astro.uni-bonn.de

<sup>2</sup> Tartu Observatory, University of Tartu, 61602 Tõravere, Tartumaa, Estonia

Received 17 December 2019 / Accepted

### ABSTRACT

**Context.** The interstellar medium is affected by turbulence and observed H I structures in channel maps are shaped by turbulent motions. It is taken for granted by a few theoreticians that observed H I structures do not represent real density enhancement but velocity caustics, caused by velocity crowding. This interpretation was questioned and objections by Clark et al. led to violent debates.

**Aims.** To settle the discussion we verify theoretical key parameters by using Effelsberg Bonn H I Survey (EBHIS) observations.

**Methods.** We apply unsharp masking to determine filamentary H I structures at high spatial frequencies. In addition we use Gaussian parameters to distinguish the cold neutral medium (CNM) from observed H I column densities. We compare power spectra and spatial distributions of dust and H I column densities, distinguishing CNM and multiphase column densities at various velocity widths.

**Results.** Observations contradict the Velocity Channel Analysis (VCA) postulate that the spectral index should steepen with the width of the velocity window. We rather find that the thin slice spectral index depends strongly on the H I phase composition. Multiphase power spectra are steeper for regions with cold gas. VCA denies such H I phase dependencies on the power distribution. Separating the CNM we find that the power spectra are significantly flatter than those for the multiphase H I composite. We observe excess CNM power for small scale structures originating from cold dust bearing filaments that are embedded in the CNM. Spectral indices for narrow channel widths depend on the Doppler temperature of the H I gas. In presence of enhanced small scale H I structure the far infrared emission from dust is also enhanced.

**Conclusions.** Small scale cold filamentary H I structures are predominantly caused by density enhancements due to phase transitions rather than by velocity caustics.

**Key words.** Turbulence – ISM: clouds – ISM: structure – (ISM:) dust, extinction

## 1. Introduction

Density distribution and motion of the interstellar medium (ISM) are affected by many influences, most notably Galactic dynamics but also turbulence is suggested to be important for all ISM constituents on all scales (Armstrong et al. 1995). The ISM contains ionized, molecular, and atomic components; here we are concerned with the neutral hydrogen (H I) which fills a large fraction of the Milky way disk and halo. The H I is easily observable and therefore an ideal tracer for various ISM structures. All sky surveys like the combined Effelsberg and Parkes H I survey (HI4PI, HI4PI Collaboration et al. 2016) or Galactic Arecibo L-Band Feed Array Survey (GALFA-H I, Peek et al. 2018) disclose a wealth of structures in data cubes that are organized in channel maps with position-position-velocity (PPV) coordinates. Comparing the new high resolution surveys with the older low resolution Leiden-Argentine-Bonn (LAB) data (Kalberla et al. 2005), one finds that the new data contain a striking wealth of previously unknown filamentary H I structures that are aligned with the magnetic field and correlated with far infrared (FIR) emission observed by *Planck* (see Clark et al. 2014, 2015; Kalberla et al. 2016; Peek et al. 2018; Clark et al. 2019; Clark, & Hensley 2019). The access to the H I survey data is easy but the interpretation is hampered by the fact that these data do not contain the full 3-D phase space information. They offer only projections

with information for two spatial coordinates perpendicular and a single one along the line of sight in velocity.

Restrictions for the turbulence analysis of such PPV data have been considered by Lazarian & Pogosyan (2000) for an isothermal medium under the assumption that the velocity field is uncorrelated with the density field. They have argued that 3-D power laws for the density field derived from PPV column density maps should depend on the width of the velocity slice used. Intensity fluctuations in thin velocity slices are affected by both, density and velocity fluctuations. In particular in case that the density spectrum is long-wave dominated, the H I intensity spectrum does not reflect the density statistics. However in the limit of very thick slices the velocity effects on the projected intensity distribution integrate out. “For thin slices the velocity fluctuations make spectra of emissivity more shallow, creating a lot of structures in position-position-velocity (PPV) space that can be erroneously identified as clouds” (Lazarian & Pogosyan 2000, Sect. 7). Such spurious structures are caused by velocity crowding along the line of sight and are called velocity caustics. Lazarian & Yuen (2018) claim that filamentary structures in thin channel maps, mentioned in the previous paragraph, and discussed in detail by Clark et al. (2014, 2015), are predominantly velocity caustics, thus fraud rather than real physical entities.

Clark et al. (2019) object against this interpretation. They consider the spatial correlation between small scale H I filaments and *Planck* 857 GHz emission (Planck 2018 results. IV. 2018)

as an indication that filamentary H I structures are true density structures in the ISM. From the fact that the best FIR/H I correlation as well as the highest FIR/H I ratio is found for cold filamentary H I structures they infer that the enhanced FIR emission is associated with colder, denser phases of the ISM. Thus structures must be caused by dust-bearing density structures and not by velocity caustics. The anisotropic cold H I structures are most obvious in thin velocity slices and are observable at high spatial frequencies. Such H I features are washed out in thick velocity slices where structures are dominated by the more extended and isotropic WNM. Changes in spectral slope are addressed to changes in the multiphase composition of the H I rather than to velocity fluctuations. [Clark et al. \(2019\)](#) conclude that thin slice spectral indices must be affected by “small-scale structure and narrow line widths typical of CNM” and call for “a significant reassessment of many observational and theoretical studies of turbulence in H I.”

[Yuen et al. \(2019\)](#) comment on [Clark et al. \(2019\)](#) and argue that thin channels always have a contribution from velocity fluctuations. They emphasize “The most valuable insight from [Lazarian & Pogosyan \(2000\)](#) is the prediction of the spectral slope change between the thin and thick PPV slices that is related to the spectral indices of turbulent velocity and density”. This is in fact the heart of the velocity channel analysis (VCA). The theory was extensively tested with numerical data, we refer to references given by [Yuen et al. \(2019\)](#). These authors admit that VCA was formulated for the isothermal gas but they argue further that temperature inhomogeneities would increase the weight of velocity related contributions to the velocity channel map, keeping the VCA phenomenon of spectral slope transitions intact. They claim that both, two phase and one phase medium show the same result. They question further that the H I filaments are indicative for cold gas and note that the data presented by [Clark et al. \(2019\)](#) are close to the North Galactic Pole where “neither formation of cold H I nor an increase of dust emissivity is likely”. Last not least [Yuen et al. \(2019\)](#) give counter examples for a particular region and question whether the relation between FIR emission and H I column density, derived by [Clark et al. \(2019\)](#), is universal.

Summing up, [Clark et al. \(2019\)](#) argue that filamentary H I structures that are preferentially aligned with the magnetic field and correlated with FIR emission are cold and dense, initiated by phase transitions and thus modifying the thin velocity channel power index. [Yuen et al. \(2019\)](#) emphasize that temperature inhomogeneities would not affect VCA, they question that filaments are cold and refer to selection effects that invalidate a general correlation between FIR emission at 857 GHz and H I column density as used by [Clark et al. \(2019\)](#).

Putting these arguments together we can work out three key questions: (i) is VCA applicable to a multiphase medium with temperature inhomogeneities and embedded cold small scale structures, (ii) how cold are H I filaments, and (iii) how good is the correlation between FIR and H I filaments?

## 2. Observations and data reduction

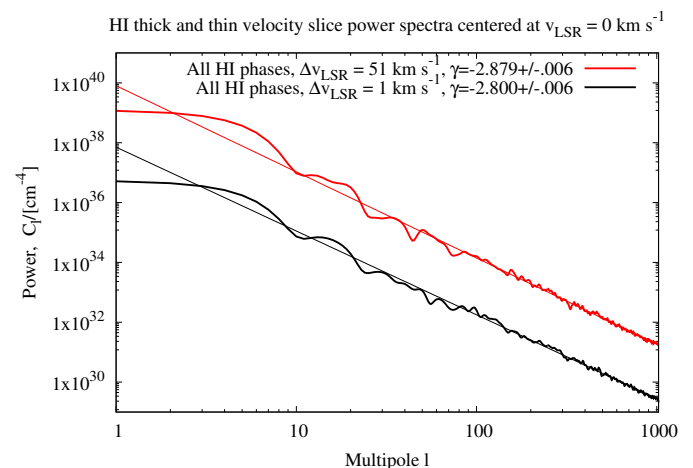
[Clark et al. \(2019\)](#) used Arecibo data. For a completely independent analysis we utilize here the Effelsberg Bonn H I Survey (EBHIS). We use for consistency the same region as [Clark et al. \(2019\)](#) and [Yuen et al. \(2019\)](#) and focus our analysis to a region with a diameter of  $15^\circ$  around longitude GAL =  $35^\circ 5$  and latitude GAB =  $54^\circ$  (RA =  $15^h 30^m 07^s$ , DEC =  $23^\circ 06' 00''$ ). For apodization we apply a cosine taper (a Tukey window, [Harris 1978](#)) and taper with a half-period of  $15^\circ$ , weighting smoothly from one to

zero for a radius  $15^\circ < R < 30^\circ$ . We calculate power spectra for velocities  $|v_{\text{LSR}}| \leq 25 \text{ km s}^{-1}$  with channel widths of  $\Delta v_{\text{LSR}} \leq 51 \text{ km s}^{-1}$  in the multipole range  $l < 1023$  ([Kalberla & Haud 2019](#)). To determine the small scale spatial structure of the H I distribution at scales of  $R < 0.5$  we apply unsharp masking (USM) ([Kalberla et al. 2016](#)). The H I data are first smoothed with a Gaussian beam of  $0.5$  at full width at half maximum, next these smooth data are subtracted from the original database to generate the USM data. In addition we use a Gaussian decomposition of the HI4PI data on an  $n_{\text{side}} = 1024$  HEALPix grid to get parameters for different phases, and distinguish between the cold, lukewarm and warm neutral medium (CNM, LNM, and WNM respectively) ([Kalberla & Haud 2018](#)).

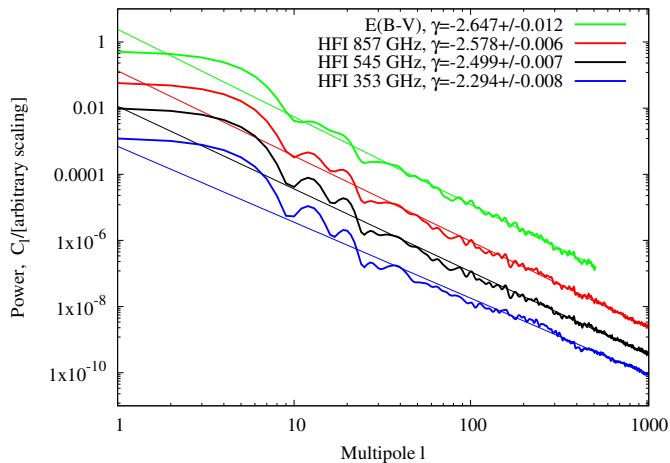
Our methods and data processing, including deep discussions of instrumental issues, are detailed by [Kalberla et al. \(2016\)](#); [Kalberla & Haud \(2018, 2019\)](#). We need to point out that the signal-to-noise level for the EBHIS is high enough to warrant a power analysis without a noise bias. For our extended analysis we use in general only data with a signal-to-noise ratio better than three, corresponding to brightness temperatures  $T_B > 0.3 \text{ K}$ . Another major advantage of our current analysis is that we use EBHIS data only, we do not need to consider complications in data processing related to different telescopes as in case of HI4PI ([Kalberla & Haud 2019](#)).

## 3. Power spectra

The Milky Way H I distribution differs from the simplified case of an isothermal, homogeneous and isotropic distribution with turbulent properties that are random and uncorrelated in density and velocity as assumed by [Lazarian & Pogosyan \(2000\)](#). In the first instance the column density of the observed H I depends strongly on position and radial velocity, next the contributions from CNM, LNM, and WNM are expected to vary a lot. In particular the cold part of the H I distribution, represented by the USM and CNM, tends to form filamentary structures with strong anisotropies, we refer to Fig. 7. If the conjecture by [Clark et al. \(2019\)](#) against caustics is correct, we should expect an imprint of these conditions to the derived power spectra.



**Fig. 1.** Power spectra of the observed H I column density distribution at  $v_{\text{LSR}} = 0 \text{ km s}^{-1}$  for an instrumental channel width of  $\Delta v_{\text{LSR}} = 1.29 \text{ km s}^{-1}$ , corresponding to the instrumental resolution (black) and for the H I integrated in the range  $-25 < v_{\text{LSR}} < 25 \text{ km s}^{-1}$  (red). Power indices from least square fits for  $l > 10$  are indicated, the indicated errors are formal one sigma uncertainties.



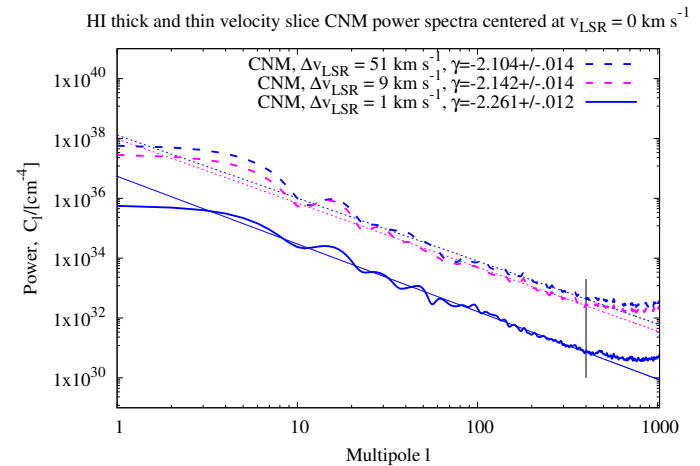
**Fig. 2.** Power spectra for E(B-V) and HFI emission at 857, 545, and 353 GHz with the corresponding least square fits.

Figure 1 shows power spectra for EBHIS data within a single channel and for column densities integrated over  $-25 < v_{\text{LSR}} < 25 \text{ km s}^{-1}$ . In both cases the spectra are straight and well defined for  $l \gtrsim 10$ , also the fits are well defined with  $\gamma = -2.800 \pm 0.006$  for the single channel and  $\gamma = -2.879 \pm 0.006$  for the thick velocity slice. The low power for  $l \lesssim 10$  reflects limitations of our field of view with a radius of  $R = 15^\circ$ , corresponding to a multipole  $l \sim 180^\circ/2R = 6$ . The power spectra are in all cases fit by us for  $l \geq 10$  only.

According to VCA the spectral indices in the limits of thin and thick velocity slices determine uniquely the spectral indices of the turbulent velocity and density fields. In case of sufficiently thick velocity slices the velocity fluctuations average out and one measures merely density fluctuations. Thin velocity slices contain in addition to density fluctuations also velocity fluctuations. These average out on large scales, hence velocity fluctuations dominate small scales and accordingly the power spectra are flattened for thin velocity slices. The difference between thin and thick slice spectral indices can then be used to determine velocity fluctuations (Yuen et al. 2019, Table 1). Taking the data presented in Fig. 1 at face value, we would conclude that the observed spectral index  $\gamma$  steepens with the width of the velocity slice as expected from theory however the difference  $\delta\gamma_{\text{VCA}} = 0.08$  is far below the expectations, indicating  $m \sim 0.16$  for the slope of velocity structure function, this is only 1/4 of  $m = 2/3$  that would be expected for Kolmogorov turbulence (Lazarian & Pogosyan 2000, Sect. 5.1).

Clark et al. (2019) compare H I data with *Planck* 857 GHz emission, assuming that gas and dust are well mixed. If this assumption is valid we would expect that H I, FIR, and reddening power spectra are compatible. We calculate power spectra for *Planck* data at 857, 545, and 353 GHz<sup>1</sup>. In addition we select E(B-V) reddening data from Schlegel et al. (1998)<sup>2</sup>. In all cases we use the same field of view and the apodization described earlier for the H I. The power spectra, shown in Fig. 2, are calculated for  $l > 10$ , the E(B-V) data are only available for  $l < 512$ . The fits for the spectral indices show a systematical flat-

tening with decreasing frequency, explainable by changes in the power distribution. The Galactic residual contribution to *Planck* power spectra is dominant at frequencies  $\nu > 217 \text{ GHz}$ , the cosmic microwave background (CMB) contribution is increasing for lower frequencies while the contribution from the cosmic infrared background (CIB) to Fig. 2 is most significant at 353 GHz (Planck intermediate results XVII. 2014, Fig. C.1). Comparing power spectra for H I with spectra for the dust distribution we note that the power spectra for the dust are well defined but have in general significantly flatter power spectra than the observed H I column densities (Fig. 1).



**Fig. 3.** As Fig. 1 but power spectra of the CNM column density distribution at  $v_{\text{LSR}} = 0 \text{ km s}^{-1}$  for  $\Delta v_{\text{LSR}} = 1.29 \text{ km s}^{-1}$  (blue solid),  $-25 < v_{\text{LSR}} < 25 \text{ km s}^{-1}$  (blue dashed), and  $-4 < v_{\text{LSR}} < 4 \text{ km s}^{-1}$  (magenta dashed). Power spectra were fit for  $10 < l < 400$ .

Clark et al. (2019) argue that dust is correlated best with cold H I filaments. If their arguments are valid we would expect that power spectra for the cold H I are in better agreement with Fig. 2 than the spectra from Fig. 1. To derive the power distribution of the cold H I we use Gaussian components for the CNM from Kalberla & Haud (2018) and Kalberla & Haud (2019) and repeat the calculation of the thin and thick slice power spectra for the CNM. The results are given in Fig. 3. Comparing the multiphase power spectra from Fig. 1 with Fig. 3 we find that the CNM power spectra are more shallow. The power is significantly reduced but at multipoles  $l \gtrsim 400$  there is a strong excess. The implication is that the H I distribution on large scales (low multipoles) is dominated by warm gas while the CNM controls small scales as claimed by Clark et al. (2019). The small scale power excess is strongest for the thin slice power spectrum. We note further that we observe at intermediate multipoles  $10 < l \lesssim 400$  a steeper CNM power spectrum in case of the thin slice, opposite to VCA expectations (Lazarian & Pogosyan 2000, Sect. 4.3). Similar results were reported by Kalberla & Haud (2019). These authors demonstrate that the power excess at high multipoles is in case of HI4PI observations not affected by noise or instrumental uncertainties. To test whether the same conditions apply to our current data analysis we calculate for comparison a CNM power spectrum for an intermediate channel width of  $-4 < v_{\text{LSR}} < 4 \text{ km s}^{-1}$ . Comparing this case with the thick velocity slice for  $-25 < v_{\text{LSR}} < 25 \text{ km s}^{-1}$  we find only slight changes in the power spectra caused by the source distribution. The CNM has most of its power at velocities close to zero. There is a slight steepening but no significant change in the power excess for  $l \gtrsim 400$ . If this excess would have been caused by un-

<sup>1</sup> HFI\_SkyMap\_857\_2048\_R3.01\_full.fits, HFI\_SkyMap\_645\_2048\_R3.01\_full.fits, and HFI\_SkyMap\_353-psb\_2048\_R3.01\_full.fits from the *Planck* Legacy Archive, <https://pla.esac.esa.int/>

<sup>2</sup> The LAMBDA Reddening (E(B-V)) Map, [https://lambda.gsfc.nasa.gov/product/foreground/fg\\_sfd\\_get.cfm](https://lambda.gsfc.nasa.gov/product/foreground/fg_sfd_get.cfm)



certainties in the data analysis we should notice an increase by a factor of 5.7 (or  $\log(5.7) = 0.75$ ), corresponding to the decrease in channel width. This is not observed.

The filamentary USM structures used by [Clark et al. \(2019\)](#) are strongly velocity dependent, we therefore expect that also power spectra for cold gas should show some velocity dependencies. To check, whether  $\gamma$  is velocity dependent, we calculate single channel power spectra for  $-25 < v_{\text{LSR}} < 25 \text{ km s}^{-1}$  for observed multiphase H I column densities and also for the CNM. The spectral indices are displayed in Fig. 4. We find fluctuations up to  $\delta\gamma \lesssim 0.5$  in case of the multiphase H I and  $\delta\gamma \lesssim 1$  in case of the CNM. The velocity dependencies are large compared to  $\delta\gamma_{\text{VCA}} = 0.08$  from Fig. 1.

Figure 4 shows three local minima in  $\gamma$ . The multiphase spectral index is steepest at  $v_{\text{LSR}} = 1 \text{ km s}^{-1}$  and the CNM power index has a local minimum at  $v_{\text{LSR}} = 0 \text{ km s}^{-1}$ . The second multiphase local minimum occurs at  $v_{\text{LSR}} = -6 \text{ km s}^{-1}$ . The thin slice power spectrum for the CNM is steepest at this velocity but still shallower than the multiphase. Significant fluctuations of the thin velocity slice spectral index with velocity are not expected for the multiphase H I in the VCA framework. Moreover, the changes in spectral index are driven by the CNM and we shall see in Sect. 5 that these fluctuations are associated with changing anisotropies (Fig. 7). The question arises whether VCA is applicable under such conditions.

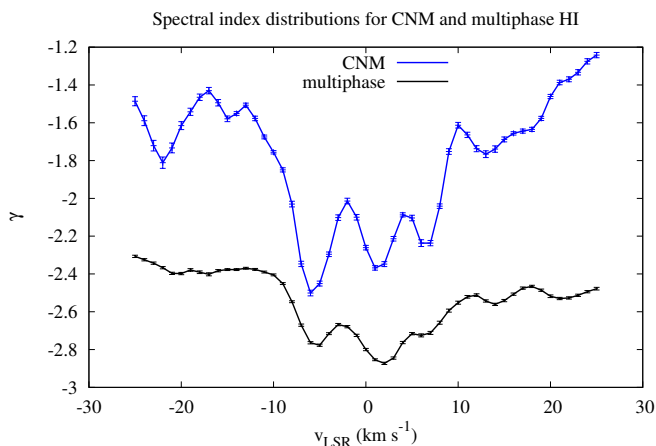


**Fig. 4.** Velocity dependent single channel power indices  $\gamma$  for the multiphase H I (black) and for the CNM (blue) with formal one sigma error bars for the fit.

Next we check the VCA key prediction that the spectral index should gradually steepen with the transition from thin to thick velocity slices. A slice is considered to be thick for a width of  $\Delta v_{\text{LSR}} \gtrsim 17 \text{ km s}^{-1}$ , as expected for warm H I at a Mach number of 1 ([Lazarian & Pogosyan 2000](#), Sect. 4.3). We calculate power spectra in slices with  $1.26 < \Delta v_{\text{LSR}} \lesssim 51 \text{ km s}^{-1}$ , a range that should cover well the transition from thin to thick velocity slices. In theory, the VCA predicted spectral steepening with velocity width should be independent of the center velocity. Observed velocity dependencies of the thin slices from Fig. 4 may imply that such dependencies can affect also the VCA and we intend to check possible dependencies of this kind. We use two of the prominent local minima from Fig. 4 with  $v_{\text{LSR}} = 0 \text{ km s}^{-1}$ , and  $v_{\text{LSR}} = -6 \text{ km s}^{-1}$ . Figure 5 displays the VCA results for the CNM only and for the observed multiphase H I.

For the multiphase H I with a center velocity  $v_{\text{LSR}} = 0 \text{ km s}^{-1}$  we see in Fig. 5 that the steepest spectral index is reached at

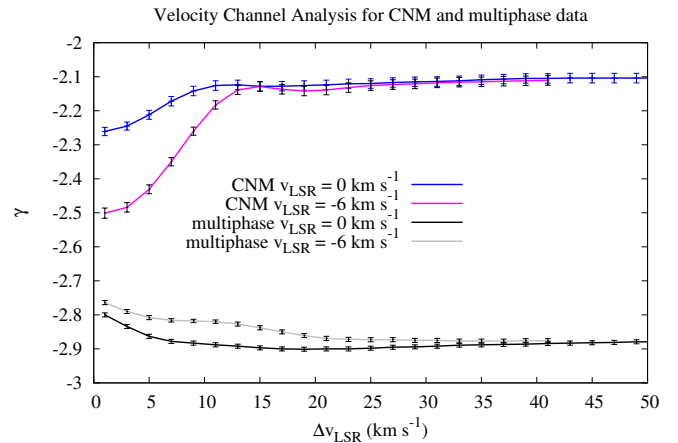


**Fig. 5.** Velocity dependent single channel power indices  $\gamma$  for the multiphase H I (black) and for the CNM (blue) with formal one sigma error bars for the fit.

$\Delta v_{\text{LSR}} \sim 17 \text{ km s}^{-1}$  but for the very thick range  $\Delta v_{\text{LSR}} \gtrsim 17 \text{ km s}^{-1}$  the power spectrum appears to flatten again. In case of a center velocity  $v_{\text{LSR}} = -6 \text{ km s}^{-1}$  the steepening is somewhat stronger but still not as significant as predicted by VCA. The result for the CNM clearly indicates that VCA is not applicable in this case. The spectral index flattens progressively with increasing  $\Delta v_{\text{LSR}}$ . The velocity dependencies, shown in Fig. 4, dominate in any case the VCA statistics for the cold H I. We have seen in Fig. 3 that most of the CNM power is concentrated at low velocities. The implication is that the surface filling factor for the CNM is largest at these velocities with a dominance of small scale structures as visible in Fig. 4.

We conclude that the objections by [Clark et al. \(2019\)](#) against VCA are justified. Spectral steepening can not be explained with a decreasing contribution of the velocity field but rather with a shallower power spectrum for the cold gas in a narrow velocity range. Thus changes in spectral index must be caused by temperature fluctuations, indicative for phase transitions.

#### 4. Doppler temperatures

In this section we want to discuss the second key question, whether H I filaments are cold as claimed by [Clark et al. \(2019\)](#). Filamentary structures discussed by [Clark et al. \(2014, 2015\)](#) are derived by unsharp masking. Low spacial frequencies are suppressed by this method but the calculations are done independently for each channel, hence velocity dependencies of the data (or correlations in velocity) remain unaltered. A priori an USM treatment should disclose small scale structure in the observed H I distribution regardless whether the observed gas is cold or warm. In other words, USM data should show fluctuations of the CNM as well as the WNM at high spatial frequencies.

For each USM structure we determine the linewidth and the corresponding Doppler temperature  $T_D$  as described by [Kalberla et al. \(2016\)](#). Alternatively we use the CNM Gaussian parameters from [Kalberla & Haud \(2019\)](#) to calculate  $T_D$ .  $T_D$  is an upper limit to the excitation or spin temperature of the H I. In both cases  $T_D$  has, as expected for a turbulent medium ([Vazquez-Semadeni 1994](#)), a log-normal distribution (e.g. [Kalberla et al. 2016](#), Fig. 13) and we determine independently for each channel of the USM and CNM data the characteristic harmonic mean Doppler temperature, Fig. 6 displays the results.

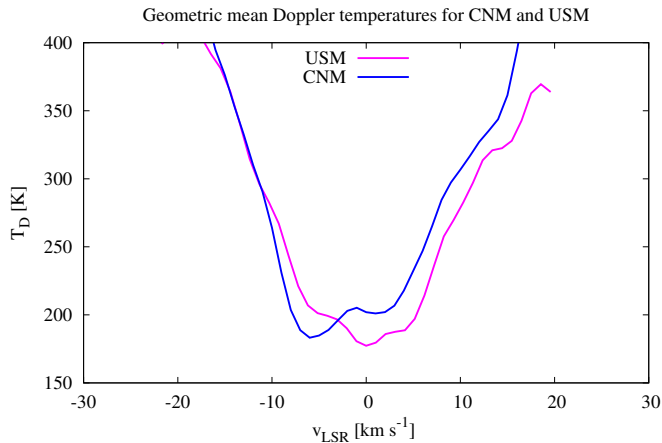


**Fig. 6.** EBHIS harmonic mean Doppler temperatures, determined from small scale USM structures and for the CNM from a Gaussian decomposition. USM data for  $v_{\text{LSR}} > 20 \text{ km s}^{-1}$  are excluded because of their low significance.

Despite the fact that selection criteria and numerical methods are very different for the determination of USM and CNM structures we find a good agreement for both independent  $T_D$  measures. A visual inspection of the data cubes confirms that USM filaments are associated with the CNM, these filaments always are located within CNM structures. USM filaments with Doppler temperatures belonging to the LNM or WNM temperature regimes were never observed though unsharp masking was extensively used for quality control of survey data observed with the Effelsberg and Parkes telescopes.

A comparison between Figs. 6 and 4 shows that the local minima in  $\gamma$ , corresponding to steeper spectral indices, are associated with cold H I filaments. The  $T_D$  curve for the USM data shows bumps that coincide with the local minima in  $\gamma$ . The agreement is less good for the CNM  $T_D$  curve. We conclude that cold H I small scale structures are responsible for the observed steepening of thin slice spectral indices. As discussed before, these structures dominate the power spectra at low velocities. Cold small scale structures may be considered as markers for phase transitions characterized by rapidly reducing kinetic energy with decreasing physical size scale (Wareing et al. 2019). Doppler temperatures  $T_D \lesssim 200 \text{ K}$  for the region discussed here are exceptional low. The all sky HI4PI median temperature is  $T_D \sim 223 \text{ K}$  (Kalberla et al. 2016) and  $T_D \sim 220 \text{ K}$  was found for the Arecibo sky (Clark et al. 2014). An inspection of Kalberla & Haud (2018, Figs. 9, 10, and 13) indicates that there is cold gas in this region. Peek & Clark (2019) used Na I absorption at high Galactic latitudes to demonstrate that small scale structures are colder than the environment.

Our results support Clark et al. (2019) and are in clear conflict with Yuen et al. (2019) who deny the existence of cold H I gas in the observed region. This section supports further the conjecture that a steepening of the spectral indices is found for particular cold H I gas condensations at small scales.

## 5. The relation between dust and cold H I gas

The third key question that we like to solve concerns the relation between dust and cold gas. The *Planck* 857 GHz dust emission is dominated by thermal dust and its intensity is proportional to dust column density which is expected to follow the H I den-

sity (Yuen et al. 2019). There appears to be a general consensus that H I gas and dust are frequently filamentary and the FIR emission is well aligned with prominent USM structures. The debate is whether these filaments indicate cold and dense gas or velocity caustics in a turbulent medium, independent of density and temperature or line width. In the previous section we have shown that USM structures are on average as cold as the CNM with Doppler temperatures even below 200 K (Fig. 6). Here we intend to explore the spatial relations between FIR, USM and CNM structures. Clark et al. (2019) demonstrated an increase of the  $I_{857}/N_{\text{HI}}$  ratio at positions with increasingly stronger USM emission. Such a relation was questioned by Yuen et al. (2019).

The power spectra in Fig. 4 have three well defined local minima. A visual inspection of the PPV cubes of the USM and CNM emission shows that these extrema are caused by the H I source distribution. We observe three major cloud complexes at velocities  $v_{\text{LSR}} \sim -6, 0$ , and  $+6 \text{ km s}^{-1}$ . Depending on velocity, the USM structures are embedded in different CNM structures. This is demonstrated in the upper panels of Fig. 7. The USM structures always follows the CNM. The lower panels show the relation between USM and FIR emission. FIR filaments are associated with distinct USM structures at different velocities and one needs to inspect all of the USM channel maps to identify counterparts between FIR and USM data. The H I distribution is very complex but on visual inspection all of the USM structures at different velocities appear to be related to FIR emission.

For a further numerical analysis of the relation between FIR and H I emission we adopt the hypothesis that all USM structures at all velocities between  $-25 < v_{\text{LSR}} < 25 \text{ km s}^{-1}$  are associated with dust, hence FIR emission at 857 GHz. We flag the FIR map at all positions with USM emission with brightness temperatures  $> 0.3 \text{ K}$  and replace the observed FIR emission with a constant background level. Following Planck intermediate results XLVIII. (2016) we determined this background level to  $1.06 \pm 0.16 \text{ MJy sr}^{-1}$  within a  $12.5$  by  $12.5$  field at ( $\text{GAL} = 90^\circ$ ,  $\text{GAB} = -80^\circ$ ) as a 857 GHz FIR background that is unaffected by USM or CNM features; we did not apply any offset corrections for warmer H I components. Figure 8 shows the results after flagging. To the left we display for comparison the observed 857 GHz FIR emission, in the middle the FIR after flagging for dust associated with USM structures. After flagging the FIR map for USM signals we repeat the calculations for CNM emission. To the right in Fig. 8 we display the results after flagging for CNM counterparts.

The middle plot of Fig. 8 shows that 83.6% of the FIR emission has been flagged under the assumption that USM and FIR emission are spatially associated. The remaining FIR flux originates close to USM structures, implying that the dust distribution is slightly more diffuse than the USM emission. Inspecting the relation between USM and CNM structures we find that the CNM is in general somewhat more extended than the USM filaments (see Fig. 7 top). FIR emission can well be related to the CNM. The result from such a hypothesis is plotted at the right hand side of Fig. 8. We find that now 99.6% of the FIR has been flagged. This ratio could even be increased by selecting a velocity range of  $-30 < v_{\text{LSR}} < 25 \text{ km s}^{-1}$ . After a visual inspection of the data we found no indications for dust associated with CNM outside this range. The remaining unflagged positions in Fig. 8, right hand side (20% of the observed field) have an average FIR flux density of  $1.07 \pm 0.18 \text{ MJy sr}^{-1}$ , consistent with our previous assumption of a  $1.06 \text{ MJy sr}^{-1}$  background level. We conclude that a significant fraction of the FIR emission originates from dust that is associated with the CNM. USM structures are spa-



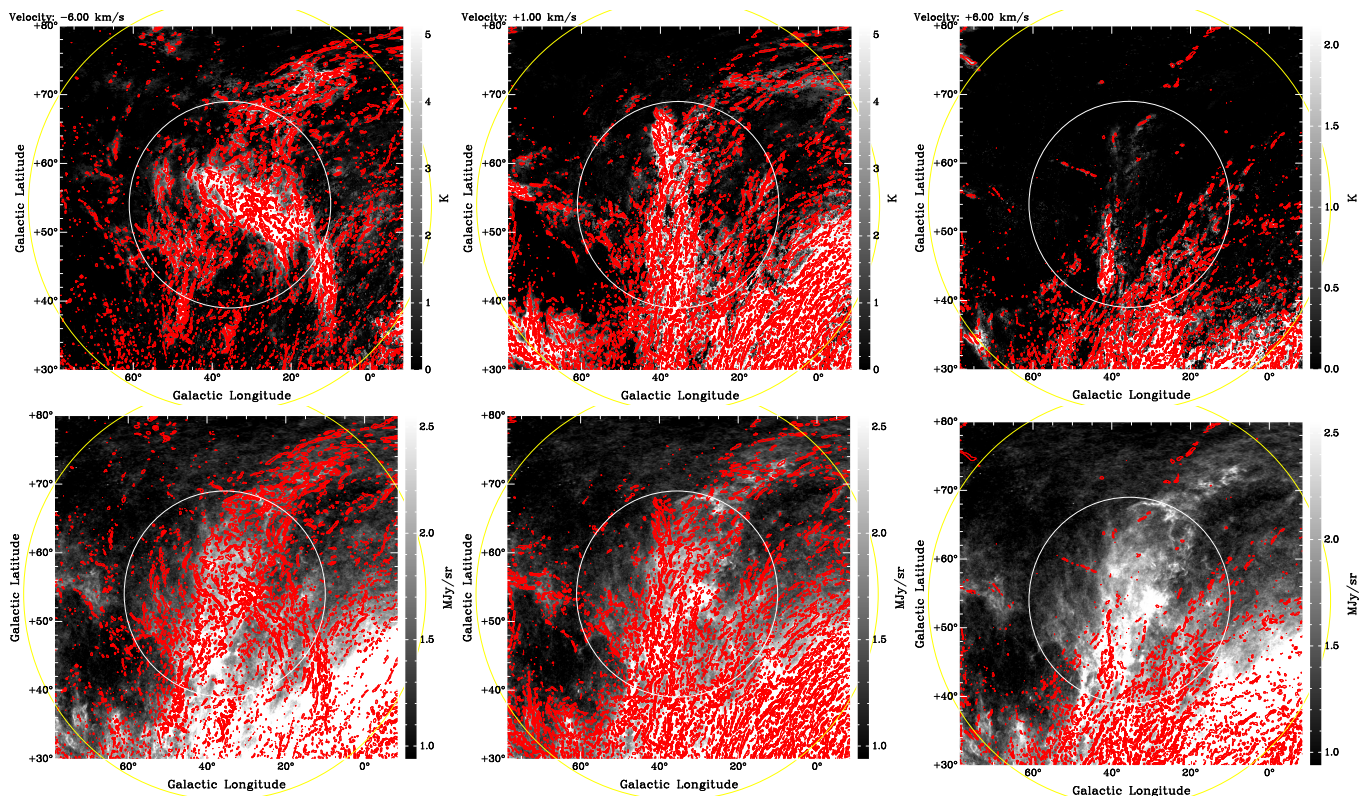


**Fig. 7.** Upper plots: CNM emission at velocities  $v_{\text{LSR}} = -6, +1$ , and  $+6$  km s $^{-1}$  from left to right, overlaid with red contours from USM emission at the same velocities with a level of  $> 0.3$  K. The lower plots show FIR emission at 857 GHz as observed by *Planck* (left), overlaid with the same USM structures as on top. The circles have radii of 15° (white) and 30° (yellow).

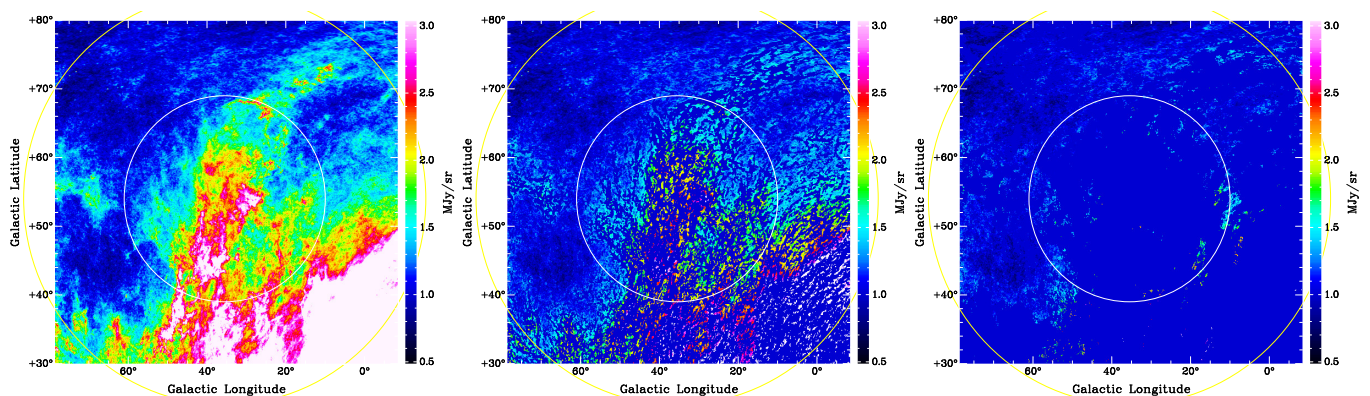


**Fig. 8.** FIR emission at 857 GHz as observed by *Planck* (left), masked in presence of USM structures (middle) and CNM emission (right) at levels of  $> 3$  K. The circles have radii of 15° (white) and 30° (yellow).

tially embedded within the CNM (see also Fig. 7) and associated with a major part (83.6%) of the dust.

After demonstrating the spatial association between dust and USM structures we want to clarify whether the  $I_{857}/N_{\text{HI}}$  ratio depends on the strength of the USM intensity as observed by Clark et al. (2019). These authors used only a fraction of the available data and restricted their analysis to the main H I component close to zero km s $^{-1}$ . Their results were questioned by Yuen et al. (2019) but these authors used also only a small 9°x 9° subset of the database. Here we want to analyze all velocities  $-25 < v_{\text{LSR}} < 25$  km s $^{-1}$  and the whole field of view. As shown by Fig. 6, the cold gas is concentrated around low velocities, therefore we integrate the column densities  $N_{\text{HI}}$  only for velocities in the range  $-25 < v_{\text{LSR}} < 25$  km s $^{-1}$ . For each position we search for USM emission at all velocities. In case that we find

several USM components at different velocities along the line of sight we assume that these components have the same  $I_{857}/N_{\text{HI}}$  ratio. This is an ambiguity in our analysis but the results do not change if we alternatively disregard such positions.

Figure 9 shows histograms for the  $I_{857}/N_{\text{HI}}$  distributions depending on lower limits  $T_u$  for USM intensities. We find that for increasing  $T_u$  (thus for more intense USM signals) the  $I_{857}/N_{\text{HI}}$  distribution shifts to higher ratios. At the same time we find a significant decrease in the total number of such features. The  $I_{857}/N_{\text{HI}}$  distribution for  $T_u = 0.3$  (all significant USM structures selected) is, as expected for a turbulent medium, approximately log-normal but this behavior breaks down for higher  $T_u$  limits. We calculate for the derived  $I_{857}/N_{\text{HI}}$  distributions the geometric mean as well as the median. Figure 10 shows that the mean ratio for  $I_{857}/N_{\text{HI}}$  is increasing continuously for an increasing  $T_u$

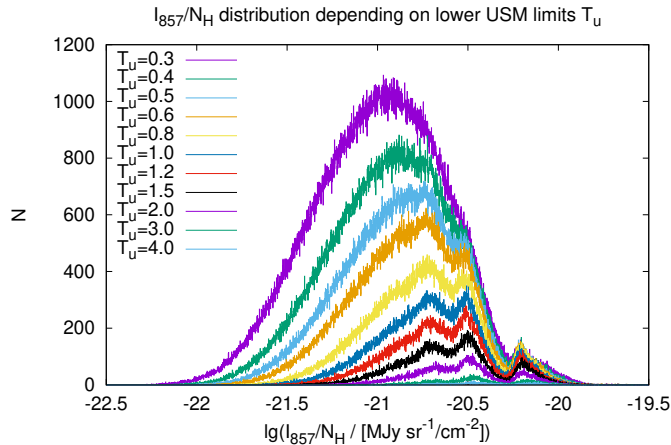


**Fig. 9.** Histograms for the  $I_{857}/N_H$  distributions as function of the lower limits  $T_u$  for the USM emission used for selecting the data.

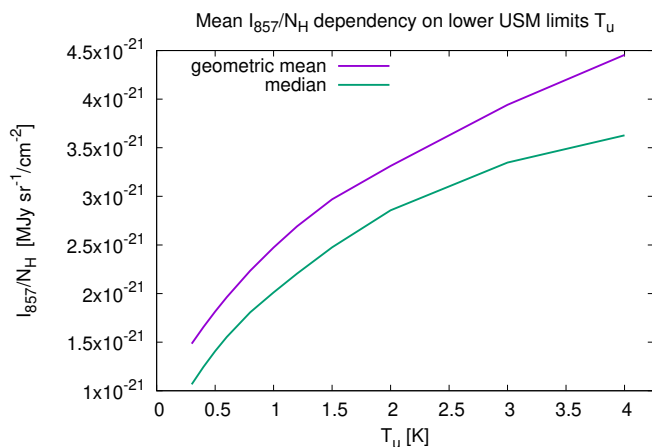


**Fig. 10.** Dependency of the  $I_{857}/N_H$  averages on the lower USM limits  $T_u$  used for Fig. 9; shown are geometric mean and median.

limit. This increase is significant, our results support the findings by [Clark et al. \(2019\)](#). May be, as stated by [Yuen et al. \(2019\)](#), that the increase of the  $I_{857}/N_H$  ratio for more pronounced USM structures is violated in some smaller specific sky patches. Such cases can not be used as an argument against global and well defined trends in a turbulent medium.

The H I distribution and in particular the USM structures can be very complex, causing difficulties for the interpretation. Figure 11 shows Renzograms for the field used by [Yuen et al. \(2019\)](#) as basis for counter arguments against [Clark et al. \(2019\)](#). Plotted are contour levels for USM intensities of 0.3 K, overplotted for each velocity channel to the FIR distribution in the background. The colors are chosen such that they represent the velocity field, from blue over green to red for negative to positive radial velocities. We see here a horrifying complicated case with numerous USM worm structures, rather complex compared to filamentary USM structures that were considered by [Clark et al. \(2019, Fig. 8\)](#).

## 6. Discussion

In Sections 3 to 5 we discussed key questions that emerged from the dispute between [Clark et al. \(2019\)](#) and [Yuen et al. \(2019\)](#) about the nature of observed H I structures. We analyzed the

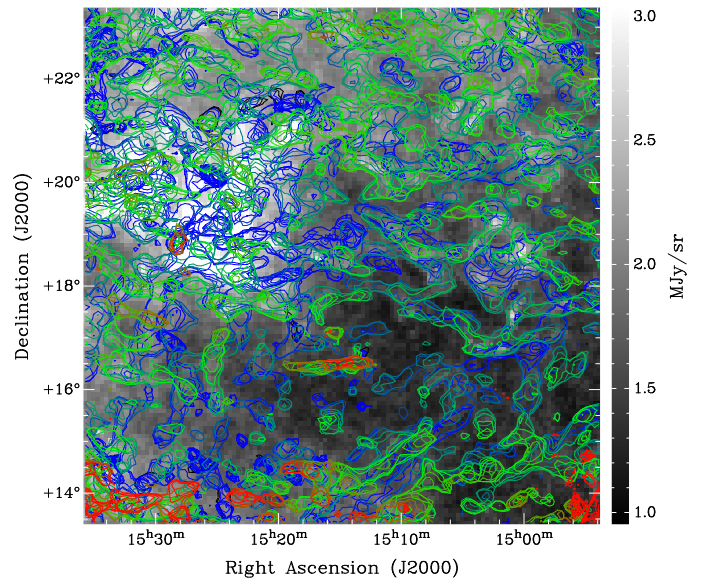


**Fig. 11.** Renzograms of USM structures in the field discussed by [Yuen et al. \(2019\)](#) at a contour level of 0.3 K, colors represent the velocity field of the USM structures. The grey scale image in the background shows the FIR emission at 857 GHz.

same region on the sky as discussed by these authors but used completely independent data from the EBHIS survey ([Winkel et al. 2016](#)). Using also different analysis tools, our intention was to verify the results under discussion. In this section we aim to broaden the discussion, taking in particular results from the literature into account that were neglected so far.

It has been stressed by [Yuen et al. \(2019\)](#) that the most valuable insight from [Lazarian & Pogosyan \(2000\)](#) is the prediction of the spectral slope change between the thin and thick PPV slices that is uniquely related to the spectral indices of turbulent velocity and density. A clear support to the VCA predictions was given by [Stanimirović & Lazarian \(2001\)](#) but on the other hand several authors found it difficult to apply VCA for an unambiguous separation of spectral indices between turbulent velocity and density in the Milky Way ([Deshpande et al. 2000](#); [Dickey et al. 2001](#); [Miville-Deschênes et al. 2003a,b](#); [Khalil et al. 2006](#); [Roy et al. 2010](#); [Pingel et al. 2018](#); [Kalberla & Kerp 2016](#); [Kalberla et al. 2017](#); [Blagrove et al. 2017](#); [Choudhuri & Roy 2019](#); [Kalberla & Haud 2019](#)). Many of these authors report that the steepening is restricted to a smaller range in velocity width ( $6 \lesssim \Delta v_{\text{LSR}} \lesssim 17 \text{ km s}^{-1}$ ) than expected ( $\Delta v_{\text{LSR}} \gtrsim 17 \text{ km s}^{-1}$ ), similar to our finding here. The conclusion is often that there is no significant change in the exponent with the velocity width of the slice. However [Yuen et al. \(2019, Table 3\)](#) re-determine spectral indices for density and velocity and draw in a few cases completely different conclusions than the authors in the original publications of [Deshpande et al. \(2000\)](#); [Khalil et al. \(2006\)](#); [Choudhuri & Roy \(2019\)](#). Unfortunately neither methods nor reasons for the updates were explained by [Yuen et al. \(2019\)](#), so we need to wait for a further publication of details that can illuminate these discrepancies. It is mandatory to explain what led to such changes. As long as clear statements are missing the new results in Table 3 of [Yuen et al. \(2019\)](#) remain questionable.

A one-to-one relation of changes in spectral slope between thin and thick PPV slices as predicted by VCA is hampered by velocity dependencies of thin slice spectral indices as observed



by Kalberla & Kerp (2016); Kalberla et al. (2017); Blagrove et al. (2017); Choudhuri & Roy (2019); Kalberla & Haud (2019). A common finding of these authors is that H I structures in channel maps can change dramatically over even small changes in velocity. Rapid intensity changes with velocity imply in any case a dominance of cold (narrow velocity width) structures. Such changes affect also the power spectra, thin slice spectral indices depend on thermal conditions. Power spectra for the multiphase H I gas steepen as the CNM contribution gets colder, suggesting that the H I phase composition is affecting the turbulent state of the H I. Simulations show that phase transitions cause steep power spectra (Wareing et al. 2019) since thermal instabilities dynamically can form sheets and filaments on typical scales of 0.1–0.3 pc. These simulations show a growth of structures, associated with a rapid rise and steepening of the density power spectra. Our conclusion from Figs. 4 and 6, consistent with findings of Kalberla & Kerp (2016); Kalberla et al. (2017); Kalberla & Haud (2019), is that the steepest multiphase power spectra are associated with particularly cold H I gas, observed as CNM and USM structures. Such thin slice power spectra show changes in spectral indices that are far stronger than the observed VCA steepening of the power spectra with velocity width as proposed by Lazarian & Pogosyan (2000) and Yuen et al. (2019). Our results support the assertion by Clark et al. (2019) that predominantly changes in the CNM content cause the observed fluctuations in spectral indices.

Caustics are caused by geometrical effects, the velocity field can push gas at the same velocity along the line of sight, mimicking density enhancements. Other geometrical considerations may offer an interpretation for the steepening of the power spectra. For optically thin gas, Lazarian & Pogosyan (2000) predict a steepening as the spatial thickness of the analyzed region increases. For a determination of the 3D power-law exponent of the underlying density field the thickness of the sampled region should be at least as large as the dimension of the map perpendicular to the line of sight. It is in general difficult to estimate the thickness of an observed H I layer, however applying these considerations to the observed steepening of the H I from Fig. 4 would imply that the depth of the thin slice multiphase H I distribution, as well as the depth of the CNM, would increase at the peak velocities for the spectral indices ( $v_{\text{LSR}} = -6, 0 +6 \text{ km s}^{-1}$ ). At the same time we observe that this gas is particularly cold (Fig. 6). A similar situation holds for other sources discussed by Kalberla & Kerp (2016); Kalberla et al. (2017). The conclusion that the extension of H I layers along the line of sight must be inverse to their Doppler temperatures appears to be so weird that a further discussion is not needed.

It was shown by Kalberla & Haud (2019) that the multiphase H I has to be considered as a phase composite with CNM, LNM, and WNM. The associated individual power spectra are correlated and differ significantly from the multiphase case. For a complete description it is necessary to take also cross correlations between these phases into account (Kalberla & Haud 2019, Eq. 4). All of the power spectra for the individual phases are shallow in comparison to the multiphase case with enhanced power for high multipoles. These are spatial frequencies where USM filaments can be observed with large single dish telescopes. Power spectra for the individual phases at intermediate multipoles  $10 \lesssim l \lesssim 100$  are more shallow and for the CNM  $\gamma_{\text{CNM}} \sim -2.4$ , in far better agreement with  $\gamma_{857} \sim -2.5$  than the average multiphase index  $\gamma_{\text{NHI}} \sim -2.9$ . Such an agreement is expected if FIR emission is correlated with CNM and USM structures as proposed by Clark et al. (2019). We have shown in Sect. 5 that the  $I_{857}/N_{\text{HI}}$  ratio increases with increasing strength

of the USM signal. The implication is that either the dust emissivity or dust-to-gas ratio is changed in filaments or that CNM filaments are associated with molecular hydrogen (Clark et al. 2019; Kalberla et al. 2020). Optical depth effects have been ruled out previously by Kalberla & Haud (2019).

Our analysis of the correlation between the FIR emission at 857 GHz and H I structures follows that of Clark et al. (2014) and Kalberla et al. (2016), we use small scale structures from USM data for correlations with FIR emission. Lazarian & Yuen (2018) identify such filaments in thin channel maps with caustics caused by velocity crowding. Following their assertion, the structures seen in Figs. 7 and 8 need to be interpreted as mere chance coincidences. Also the observed dependencies between the  $I_{857}/N_{\text{HI}}$  ratio and the strength of the USM signal can not be explained in this context. We have shown in Fig. 6 that both, USM and CNM structures are cold, a finding that was also questioned by Yuen et al. (2019). Searching for an interpretation of the  $I_{857}/N_{\text{HI}}$  ratio in context with the warmer part of the multiphase H I distribution leads to considerable difficulties, we refer to the most recent analysis of the large-scale distribution of interstellar reddening derived from H I emission by Lenz et al. (2017) and further references discussed by these authors. The gas-to-dust ratio is well defined only for  $N_{\text{HI}} \lesssim 4 \cdot 10^{20} \text{ cm}^{-2}$  and  $E(B - V) \lesssim 0.08 \text{ mag}$ . Figure 9 of Lenz et al. (2017) shows that USM and CNM structures in Figs. 7 and 8 belong to a multiphase medium that is mostly out of this range. Variations in the gas-to-dust ratio are a long standing problem. Liszt (2014) attributed systematic trends in the gas-to-dust ratio to the onset of H<sub>2</sub> formation at low temperatures. In view of these results our argumentation got circular. Trying to explain the  $I_{857}/N_{\text{HI}}$  ratio in context with the multiphase H I distribution we end up with suggestions by Clark et al. (2019), previously rejected by Yuen et al. (2019), that point to the coldest H I components. VCA considers basically a WNM dominated H I fluid at Mach one, and the properties of the embedded CNM are inconsistent with such an approach.

There remains to be explained why the velocity width dependent power spectral indices derived by Stanimirović & Lazarian (2001) are in perfect agreement with the VCA theory by Lazarian & Pogosyan (2000). The derived power spectra come from the observed H I layer of the small Magellanic cloud, extending roughly perpendicular to the line of sight with scales between 30 pc and 4 kpc. In our case, Fig. 3 shows excess power for the CNM at  $l \gtrsim 400$ , corresponding to scales  $\lesssim 0.5$ . This corresponds to the angular scale that was used by us to filter USM structures and corresponds to a linear scale of 1 pc at an assumed distance of 100 pc. Filamentary H I structures were previously reported to have extensions well below a parsec (Clark et al. 2014; Kalberla et al. 2016). These are also scales where phase transitions are expected (Audit & Hennebelle 2005; Federrath 2016; Wareing et al. 2019). Observations with a beam width of more than 30 times this scale can not resolve phase fluctuations within the H I layer (imagine what kind of Milky Way ISM research you can do with a 3.3 m dish in place of a 100 m dish). The power analysis for the SMC is sensitive to fluctuations of the total H I column density, to be considered observationally as a single phase only. This is exactly the condition assumed by Lazarian & Pogosyan (2000) and the findings of Stanimirović & Lazarian (2001) provide a direct prove for VCA. In case of the Galactic H I the single phase assumption is violated and VCA does not apply. The statement by Yuen et al. (2019) that “both two phase and one phase show the same result” is not supported by observations. Fluctuations in spectral indices observed for H I



in the Milky Way are predominantly affected by fluctuations in the phase composition. We can not exclude VCA predicted influences from velocity fluctuations but these must be marginal compared to changes in spectral index caused by temperature dependencies from the CNM. Accordingly velocity caustics must be marginal and observed filamentary H I structures are caused predominantly by dust-bearing density structures as proposed by (Clark et al. 2019).

## 7. Summary

Intending to moderate the discussion between (Clark et al. 2019) and Yuen et al. (2019) whether H I filaments are dust-bearing density structures or velocity caustics, we analyzed EBHIS data from the same region around (GAL= 35°5, GAB= 54°) as used by these authors. We used unsharp masking to determine filamentary H I structures at high spatial frequencies. These structures are cold and associated with FIR emission from dust at 857 GHz. We also use a Gaussian decomposition to extract CNM structures. The USM emission is found to be embedded within the CNM. While the FIR emission is slightly more extended than the USM emission we find that the CNM covers all FIR emission traced by the USM structures. We confirm the results by Clark et al. (2019) that the  $I_{857}/N_{HI}$  ratio is elevated in regions with strong USM emission, implying that these structures are density enhancements.

We test the VCA hypothesis that H I filaments originate from velocity caustics, caused by velocity crowding along the line of sight. We calculate power spectra for FIR emission, observed H I column densities, and also for the CNM. The single channel H I power spectra are steepest at velocities where the USM structures as well as the CNM is coldest. At these velocities the 857 GHz power spectrum ( $\gamma_{857} \sim -2.58$ ) shows the best agreement with the steepest CNM power spectrum ( $\gamma_{CNM} \sim -2.5$  at  $v_{LSR} = -6 \text{ km s}^{-1}$ ). For single channel power spectra we find power index fluctuations up to  $\delta\gamma \lesssim 0.5$  in case of the multiphase H I and  $\delta\gamma \lesssim 1$  in case of the CNM. These velocity dependencies are large compared to the steepening  $\delta\gamma_{VCA} = 0.08$  caused by a transition from thin to thick velocity slices. The VCA predicted steepening is marginal in comparison to thin slice index fluctuations that do not exist for an isothermal medium. We find that the spectral index for the multiphase medium is steepest at those velocities where the CNM or USM emission is coldest. Such a coincidence supports an explanation by phase transitions. These lead to a local decrease of the thermal line widths but the column densities do not change significantly. Thus, thermal instabilities produce enhanced power in the line centers of the observed H I at the expense of the power in the wings of the line. Thermal instabilities occur predominantly at small scales, condensations from WNM to CNM thus decrease the multiphase power predominantly at high multipoles. In consequence the multiphase power spectra steepen, a process that was observed during simulations by Wareing et al. (2019). CNM power spectra are affected in the opposite sense. Phase transition at small scales increase the power at high multipoles, leading to shallower power spectra.

Our results, in agreement with (Clark et al. 2019), call for a significant reassessment of many observational and theoretical studies of turbulence in H I, emphasizing in particular on the response from phase transitions. The VCA theory by Lazarian & Pogosyan (2000) is one of the most important contributions to our understanding of the turbulent ISM and inspired hundreds of publications in this field. We do not want to question the validity of VCA in regions that are dominated by the WNM. The reported discrepancies between theory and observations hamper

our understanding of the relations between cold filamentary gas and dust and need urgently be solved.

Comments and discussions in this paper are based on the version of Yuen et al. (2019) as submitted on 5 Apr 2019 to arXiv, available at the time of submission of our contribution. Currently there are six citations registered by ADS, the contributions by Yuen et al. (2019) appear to spread out quickly and we like to argue against theoretical concepts that are opposed by observations.

*Acknowledgements.* P. K. thanks Jürgen Kerp for support and discussions. U. H. acknowledges the support by the Estonian Research Council grant IUT26-2, and by the European Regional Development Fund (TK133). This research has made use of NASA's Astrophysics Data System. EBHIS is based on observations with the 100-m telescope of the MPIfR (Max-Planck-Institut für Radioastronomie) at Effelsberg. Some of the results in this paper have been derived using the HEALPix package. We also used the Karma package by R.E. Gooch.

## References

- Armstrong, J. W., Rickett, B. J., & Spangler, S. R. 1995, *ApJ*, 443, 209
- Audit, E., & Hennebelle, P. 2005, *A&A*, 433, 1
- Blagrove, K., Martin, P. G., Joncas, G., et al. 2017, *ApJ*, 834, 126
- Choudhuri, S., & Roy, N. 2019, *MNRAS*, 483, 3437
- Clark, S. E., Peek, J. E. G., & Putman, M. E. 2014, *ApJ*, 789, 82
- Clark, S. E., Hill, J. C., Peek, J. E. G., et al. 2015, *Phys. Rev. Lett.*, 115, 241302
- Clark, S. E., Peek, J. E. G., & Miville-Deschênes, M.-A. 2019, *ApJ*, 874, 171
- Clark, S. E., & Hensley, B. S. 2019, arXiv e-prints, arXiv:1909.11673
- Dickey, J. M., McClure-Griffiths, N. M., Stanimirović, S., Gaensler, B. M., & Green, A. J. 2001, *ApJ*, 561, 264
- Deshpande, A. A., Dwarakanath, K. S., & Goss, W. M. 2000, *ApJ*, 543, 227
- Federrath, C. 2016, *MNRAS*, 457, 375
- Harris, F. J. 1978, *IEEE Proceedings*, 66, 51
- HI4PI Collaboration, Ben Bekhti, N., Flöer, L., et al. 2016, *A&A*, 594, A116
- Kalberla, P. M. W., Burton, W. B., Hartmann, D., et al. 2005, *A&A*, 440, 775
- Kalberla, P. M. W., Kerp, J., Haud, U., et al. 2016, *ApJ*, 821, 117
- Kalberla, P. M. W., & Kerp, J. 2016, *A&A*, 595, A37
- Kalberla, P. M. W., Kerp, J., Haud, U., & Haverkorn, M. 2017, *A&A*, 607, A15
- Kalberla, P. M. W., & Haud, U. 2018, *A&A*, 619, A58
- Kalberla, P. M. W., & Haud, U. 2019, *A&A*, 627, A112
- Kalberla, P. M. W., Kerp, J., Haud, U. *A&A*, submitted
- Khalil, A., Joncas, G., Nekka, F., Kestener, P., & Arneodo, A. 2006, *ApJS*, 165, 512
- Lazarian, A., & Pogosyan, D. 2000, *ApJ*, 537, 720
- Lazarian, A., & Yuen, K. H. 2018, *ApJ*, 853, 96
- Lenz, D., Hensley, B. S., & Doré, O. 2017, *ApJ*, 846, 38
- Liszt, H. 2014b, *ApJ*, 783, 17
- Martin, P. G., Blagrove, K. P. M., Lockman, F. J., et al. 2015, *ApJ*, 809, 153
- Miville-Deschênes, M.-A., Joncas, G., Falgarone, E., & Boulanger, F. 2003, *A&A*, 411, 109
- Miville-Deschênes, M.-A., Levrier, F., & Falgarone, E. 2003, *ApJ*, 593, 831
- Miville-Deschênes, M.-A., & Martin, P. G. 2007, *A&A*, 469, 189
- Peek, J. E. G., Babler, B. L., Zheng, Y., et al. 2018, *ApJS*, 234, 2
- Peek, J. E. G., & Clark, S. E. 2019, *ApJ*, 886, L13
- Pingel, N. M., Lee, M.-Y., Burkhart, B., & Stanimirović, S. 2018, *ApJ*, 856, 136
- Planck Collaboration, Abergel, A., Ade, P. A. R., et al. 2014, *A&A*, 566, A55
- Planck intermediate results. XXX. 2016, *A&A*, 586, A133
- Planck Collaboration, Aghanim, N., Ashdown, M., et al. 2016, *A&A*, 596, A109
- Planck Collaboration, Akrami, Y., Ashdown, M., et al. 2018, arXiv e-prints, arXiv:1807.06208
- Roy, N., Chengalur, J. N., Dutta, P., & Bharadwaj, S. 2010, *MNRAS*, 404, L45
- Roy, N., Minter, A. H., Goss, W. M., Brogan, C. L., & Lazio, T. J. W. 2012, *ApJ*, 749, 144
- Saury, E., Miville-Deschênes, M.-A., Hennebelle, P., Audit, E., & Schmidt, W. 2014, *A&A*, 567, A16
- Schlegel, D. J., Finkbeiner, D. P., & Davis, M. 1998, *ApJ*, 500, 525
- Stanimirović, S., Staveley-Smith, L., Dickey, J. M., Sault, R. J., & Snowden, S. L. 1999, *MNRAS*, 302, 417
- Stanimirović, S., & Lazarian, A. 2001, *ApJ*, 551, L53
- Vazquez-Semadeni, E. 1994, *ApJ*, 423, 681
- Wareing, C. J., Falle, S. A. E. G., & Pittard, J. M. 2019, *MNRAS*, 485, 4686
- Winkel, B., Kerp, J., Flöer, L., et al. 2016, *A&A*, 585, A41
- Yuen, K. H., Hu, Y., Lazarian, A., & Pogosyan, D. 2019, arXiv:1904.03173